

Causes and underlying dynamic processes of the mid-winter suppression in the North Pacific storm track

Yuanbing ZHAO¹ & X. San LIANG^{1,2*}¹ School of Atmospheric Sciences, Nanjing University of Information Science and Technology, Nanjing 210044, China;² School of Marine Sciences, Nanjing University of Information Science and Technology, Nanjing 210044, China

Received February 3, 2018; revised August 27, 2018; accepted November 20, 2018; published online February 28, 2019

Abstract Baroclinic wave activity in the North Pacific exhibit peaks in late fall and early spring, and a local minimum in midwinter, when by linear baroclinic instability theory it should attain its maximum. This counterintuitive phenomenon, or “midwinter suppression” (MWM) as called, is investigated with a functional analysis apparatus, multiscale window transform (MWT), and the MWT-based theory of canonical transfer and localized multi-scale energetics analysis, together with a feature tracking technique, using the data from the European Centre for Medium-Range Weather Forecasts ReAnalysis (ERA-40). It is found that the MWM results from a variety of different physical processes, including baroclinic canonical transfer, diabatic effect, energy flux divergence, and frictional dissipation. On one hand, baroclinic canonical transfer and diabatic effect achieve their respective maxima in late fall. More transient available potential energy is produced and then converted to transient kinetic energy, resulting in a stronger storm track in late fall than in midwinter. On the other hand, in early spring, although baroclinic instability and buoyancy conversion are weak, energy flux convergences are substantially strengthened, leading to a net energy inflow into the storm track. Meanwhile, frictional dissipation is greatly reduced in spring; as a result, less transient energy is dissipated in early spring than in midwinter. It is further found that the weakening of baroclinic canonical transfer in midwinter (compared to late fall) is due to the far distance between the storm and the jet stream (located at its southernmost point), which suppresses the interaction between them. Regarding the increase in energy flux convergence in early spring, it appears to originate from the increase (enhancement) in the number (strength) of storms from the upstream into the Pacific.

Keywords Storm track, Midwinter suppression, Multiscale window transform, Multiscale energetics, Canonical transfer, Energy flux convergence

Citation: Zhao Y, Liang X. 2019. Causes and underlying dynamic processes of the mid-winter suppression in the North Pacific storm track. *Science China Earth Sciences*, 62: 872–890, <https://doi.org/10.1007/s11430-018-9310-5>

1. Introduction

Atmospheric storm tracks are geographical locations of bandpass transient variance maxima, or simply the preferred regions of storm (cyclone) activity (Blackmon et al., 1977). In the Northern Hemisphere, there exist two major storm tracks, namely, the Pacific and Atlantic storm tracks (Blackmon et al., 1977; Hoskins and Hodges, 2002; Chang et al., 2002; Zhu and Sun, 1999). Within the storm track, sy-

notic disturbances occur frequently and propagate eastward. These disturbances have been believed to be baroclinic waves (Charney, 1947; Lim and Wallace, 1991), and play a vital role in the transportation of momentum, heat, and material (e.g., water vapor) and in the balance of mass and energy across different latitudes. According to the theory of linear baroclinic instability, the maximum baroclinic growth rate of these systems can be expressed as

$$\sigma = 0.31 \frac{f}{N} \frac{\partial \bar{u}}{\partial z}, \quad (1)$$

where \bar{u} is the mean zonal wind, f is the Coriolis parameter,

* Corresponding author (email: san@pacific.harvard.edu)

and N is the buoyancy frequency (e.g., Eady, 1949; Lindzen and Farrell, 1980). It is thus reasonable to assume that synoptic systems, and the storm track they produce, would both be strongest in winter when the atmospheric baroclinicity is the largest in the year. However, Nakamura (1992) found that the Pacific storm track is actually weaker in midwinter than in late fall and early spring, countering what one would expect. He called this unusual phenomenon the midwinter suppression or the midwinter minimum (MWM). Since then, MWM has also been identified in a variety of observations (e.g. Christoph et al., 1997; Chang, 2003), and successfully simulated in atmospheric general circulation models (e.g., Zhang and Held, 1999; Robinson and Black, 2005; Park et al., 2010).

Since the discovery of MWM, a lot of effort has been devoted to understanding its underlying dynamics. Nakamura (1992) found that, when the wind speed at the jet center is less than 45 m s^{-1} , the intensity of storm activity in the northwestern Pacific is positively correlated with the jet strength; otherwise, they are negatively correlated. Later, similar relations have also been found in the general circulation model (Christoph et al., 1997). Nakamura (1992) argued that when the jet becomes extremely strong, the accompanying strong advection can make the systems move faster through the strong baroclinic zone, which is not conducive to tapping the available potential energy from the background field, and thus reducing the spatial growth rate of the disturbance. Chang (2001) calculated the moving speed of the wave packet in the storm track and found that the strengthening of the jet speed in winter can increase the wave packet speed by about 50%. However, Nakamura et al. (2002) and Harnik and Chang (2004) later argued that the maximum baroclinic growth rate is also increasing as the jet strengthens. Moreover, the increase in maximum baroclinic growth rate is large enough to offset the decrease in the spatial growth rate caused by the strong advection. On the other hand, some studies (Nakamura, 1992; Chang, 2001; Nakamura and Sampe, 2002; Harnik and Chang, 2004) pointed out that super strong jet may alter the structure of the baroclinic waves, lowering the correlation between the temperature perturbation and meridional (or vertical) wind perturbation, which can reduce the efficiency of the disturbance to obtain energy from the background flow.

Based on energetics diagnostics, Deng and Mak (2005, 2006) found that both baroclinic transfer and barotropic transfer are strengthened in winter, but the latter is stronger than the former. Therefore, as they concluded, the MWM is caused by the anomalous enhancement of the inverse kinetic energy (KE) transfer in winter. However, other studies (Chang, 2001; Yin, 2002; Chang and Zurita-Gotor, 2007; Chen et al., 2013) found that the inverse KE transfer in the Pacific storm track is actually weaker in winter than in late fall and early spring, and, consequently, the inverse KE

transfer cannot be the primary cause of the MWM.

Upstream seeding has also been identified as a factor closely related to the midwinter suppression of the Pacific storm track. For example, the lee-side cyclones east of the Altai-Sayan Mountains are found to be fewer in winter than in fall and spring (Chen et al., 1991); Nakamura (1992) speculated that the suppression may result from the variation of the upstream Rossby wave activity; Newton (2004) identified a significant correlation between the number of cyclones generated east of the Altai-Sayan Mountains and the Pacific storm-track strength; Robinson and Black (2006) found that the amplitude of the disturbance from the upstream into the Pacific storm track is smaller in winter than in spring and fall. Using a general circulation model, Park et al. (2010) and Lee et al. (2013) observed that the presence of Asian mountains can suppress the baroclinic energy release globally (especially in East Asia) in winter, and hence decreases the number of storms entering the Pacific storm track. Recently, based on an eddy-tracking technique, Penny et al. (2010, 2011) studied the relationship between the upstream seeding and the MWM, and found that the number (intensity) of storms entering the storm track from Siberia decreased (weakened) in winter, leading to the formation of MWM. However, using the same eddy-tracking method, Chang and Guo (2011, 2012) did not find significant correlation between the intensity of the upstream seeding and the intensity of the downstream storm track throughout the cold season (January to April), so did Zhang (1997) with the general circulation model, which, nonetheless, reproduced successfully the phenomenon of MWM.

Several studies have examined the regulation of diabatic processes in the seasonal variation of the Pacific storm track and its role in the MWM (Chang, 2001; Lee et al., 2011). Chang (2001) found via numerical experiments that the diabatic process produces eddy available potential energy (APE) in spring and fall, while in winter it consumes APE. Chang and Zurita-Gotor (2007) argued that dry processes (such as barotropic deformation) alone cannot explain the formation of MWM; diabatic processes must be taken into account. Recently, Yao et al. (2018) found that the variation of the intensity of the sub-polar oceanic front plays an important role.

As can be seen from the above, a variety of mechanisms have been proposed to interpret the formation of MWM of the North Pacific storm track, but so far as of today, none has been well accepted as the fundamental one. On the other hand, it has been argued that MWM actually results from a combination of several mechanisms, rather than from one single mechanism (Penny et al., 2010; Chang and Guo, 2011). How different mechanisms collaborate to produce the MWM in the North Pacific storm track is hence worthwhile to investigate. This study attempts to fulfill this goal. We will analyze the dynamical processes underlying the MWM,

using a recently developed localized multi-scale energetics analysis method, and through the analysis identify the primary mechanisms that lead to the formation of the unusual phenomenon.

2. Data

In this study the 40-year European Centre for Medium-Range Weather Forecasts (ECWMF) ERA-40 reanalysis dataset (Uppala et al. 2005; <http://apps.ecmwf.int/datasets/data/era40-daily/levtype=pl/>) is used. This dataset has been widely used for atmospheric researches (e.g., Chang and Guo, 2007; Penny et al., 2010). It has a horizontal resolution of $2.5^\circ \times 2.5^\circ$, and a temporal resolution of 6 h. Vertically it has 23 levels, from 1000 hPa to 1 hPa. The duration is from September 1957 to July 2002. The fields of velocity components (u , v , w), geopotential (ϕ), and temperature (T) for the entire North Pacific region (120°E – 120°W , 20°N – 70°N) will be used.

3. Methods

3.1 Multiscale window transform, canonical transfer, and multiscale energetics

Traditionally the widely used multiscale energetics are formulated through Reynolds decomposition, which, if with respect to time (space), invokes a hidden assumption of stationarity (homogeneity). However, real atmospheric processes, the storm activity considered here in particular, are in nature not stationary, and generally not homogeneous. During the past decades, it has been popular to use filters to replace the Reynolds decomposition in order to represent the highly localized energy burst processes. But in these formalisms, a fundamental issue is yet to be resolved. That is, in such a formalism, what is multiscale energy and how is it represented? Unfortunately, this problem has all been overlooked (or even not realized) in the past decades. A common practice is simply to take the square of a filtered field (up to some multiplier) as the energy. This is, unfortunately, conceptually wrong (see below), as multiscale energy is a concept in phase space, while filtered fields are physical space variables; they are linked through the Parseval identity in functional analysis (Liang 2016). In the second section of Xu and Liang (2017), we have given a brief illustration of this problem with the aid of a simple pair of Fourier coefficients. In the following we reintroduce the illustration, in order to provide an easy reference here.

Considering a velocity field $u(t)$, we can decompose it into two components: $u = u_L + u_H$ using a classical filter, where u_L and u_H , are called the low- and high-frequency reconstructions, respectively; they represent the low- and high-pass

processes. It is frequently seen in the literature that the energy of these two parts has been directly taken as u_L^2 and u_H^2 . This is conceptually wrong. For example, if $u(t)$ involves only two harmonics with frequencies ω_0 and ω_1 :

$$u = \underbrace{(a_0 \cos \omega_0 t + b_0 \sin \omega_0 t)}_{u_L} + \underbrace{(a_1 \cos \omega_1 t + b_1 \sin \omega_1 t)}_{u_H}, \quad (2)$$

then the energies of these two parts should be the sum of the squares of their respective Fourier transform coefficients $a_0^2 + b_0^2$ and $a_1^2 + b_1^2$, rather than u_L^2 and u_H^2 . In fact, the former two, i.e., $a_0^2 + b_0^2$ and $a_1^2 + b_1^2$, are constants, whereas the latter two, i.e., u_L^2 and u_H^2 , are variables of time. They cannot be equal at all. How to represent multiscale energy with its local features preserved is therefore by no means as trivial a task as those in many publications during the past decades. In fact, this has been hopeless until wavelets and filter banks are connected (Strang and Nguyen, 1997).

In 2007, Liang and Anderson developed a tool, called multiscale window transform (MWT), and solved the above problem. MWT allows us to decompose a function space into a direct sum of orthogonal subspaces, each with an exclusive range of scales, while retaining the locality of the resulting multiscale energies. Liang and Anderson (2007) termed such a subspace a scale window, or simply a window. They found that, for some specially constructed orthogonal filters, there exists a transfer-reconstruction pair, just as the Fourier transform and inverse Fourier transform: multiscale window transform and multiscale window reconstruction. The former is MWT, and the latter is shortened as MWR. MWR functions like a filter. For a series $S(t)$, application of MWR results in a filtered series, written $S^{\sim \varpi}(t)$ (ϖ indicates which window it is), while application of MWT to it gives the corresponding MWT coefficients, written $\tilde{S}_n^{\sim \varpi}$ ($\tilde{(\cdot)}_n^{\sim \varpi}$ denotes MWT on window ϖ at time step n). Multiscale energy cannot be represented using the filtered series $S^{\sim \varpi}(t)$, but can be expressed in terms of $\tilde{S}_n^{\sim \varpi}$ the MWT coefficients, thanks to an established property, Property of Marginalization (Liang and Anderson, 2007). So with MWT, the multiscale energy can be naturally expressed in terms of the transform coefficients. This is where MWT is quite different from the traditional filters.

In application, scale windows should be first defined. Following Liang and Anderson (2007), it is defined by two scale levels on the wavelet spectrum. These scale levels are called window bounds. Given a time series $S(t)$ with a duration τ , a scale level j corresponds to a period $2^{-j}\tau$. For the purpose of this study, we need two scale windows, i.e., a low-frequency background window and a synoptic window. Hence one scale level j_1 suffices to fulfil the scale window demarcation. The processes with a characteristic time scale longer than $2^{-j_1}\tau$ will be put into the background window,

whereas the remaining part belongs to the synoptic window. Here we choose 16 days, instead of 6 or 10 days as often seen in the literature, as the window bound, because previous studies (e.g., Anderson et al., 2003) indicate that the 2.5–6-day band-pass or 10-day high-pass filtered field cannot fully single out the midlatitude storm signal from the total field (see also Chang, 1993), and, to be worse, may even have a detrimental impact on individual weather systems. Besides, MWT requires that the number of time steps be a power of 2. For convenience, the low-frequency background window and the synoptic window will be denoted by $\varpi=0,1$ respectively.

Following Liang (2016), consider the primitive equations in pressure coordinates:

$$\frac{\partial \mathbf{v}_h}{\partial t} + \mathbf{v}_h \cdot \nabla_h \mathbf{v}_h + \omega \frac{\partial \mathbf{v}_h}{\partial p} + f \mathbf{k} \times \mathbf{v}_h = -\nabla_h \Phi + \mathbf{F}, \quad (3)$$

$$\frac{\partial \Phi}{\partial p} = -\alpha, \quad (4)$$

$$\nabla_h \cdot \mathbf{v}_h + \frac{\partial \omega}{\partial p} = 0, \quad (5)$$

$$\frac{\partial T}{\partial t} + \mathbf{v}_h \cdot \nabla_h T + \omega \frac{\partial T}{\partial p} + \omega \alpha \frac{L-L_d}{g} = \frac{\dot{q}_{\text{net}}}{c_p}, \quad (6)$$

$$p\alpha = RT, \quad (7)$$

where $\mathbf{v}_h=(u, v)$ is the horizontal velocity vector, $\omega=dp/dt$; f is the Coriolis parameter, ∇_h is the horizontal divergence

operator, \mathbf{F} represents all processes of external forcing and dissipation, T is temperature anomaly (with the mean profile $T(p)$ removed), L is the lapse rate and L_d the lapse rate for dry air, c_p is the specific heat capacity of air for isobaric processes, and \dot{q} is the net diabatic heating rate. Other symbols are conventional. From these equations, Liang (2016) obtained the equations governing the kinetic energy (KE) and available potential energy (APE) on the two scale windows ($\varpi=0,1$),

$$\frac{\partial A^\varpi}{\partial t} + \nabla \cdot \mathbf{Q}_A^\varpi = \Gamma_A^\varpi - b^\varpi + S_A^\varpi + F_A^\varpi, \quad (8)$$

$$\frac{\partial K^\varpi}{\partial t} + \nabla \cdot \mathbf{Q}_K^\varpi = \Gamma_K^\varpi - \nabla \cdot \mathbf{Q}_P^\varpi + b^\varpi + F_K^\varpi. \quad (9)$$

Table 1 lists the mathematical expressions and physical explanations for the respective terms. (Note here the time step n has been suppressed for notational brevity). Among them, the Γ terms are of particular importance; they represent the energy transfers between different scale windows, and possess an interesting property:

$$\sum_{\varpi} \sum_n \Gamma_n^\varpi = 0, \quad (10)$$

(now the subscript n is supplied). This property was first speculated in Liang and Robinson (2005) and later on rigorously proved (see Liang, 2016). Physically it means that this kind of energy transfer is a mere redistribution of energy among the scale windows; it must be such that energy as a whole be conserved. This conservation law distinguishes our

Table 1 The expressions and interpretations for the energetics terms in eqs. (6)–(7)^{a)}

Symbol	Mathematical expression	Physical interpretation
K^ϖ	$\frac{1}{2} \tilde{\mathbf{v}}_h \cdot \tilde{\mathbf{v}}_h$	KE on window ϖ
\mathbf{Q}_K^ϖ	$\frac{1}{2} (\tilde{\mathbf{v}}_h \tilde{\mathbf{v}}_h) \cdot \tilde{\mathbf{v}}_h$	KE flux on window ϖ
Γ_K^ϖ	$\frac{1}{2} [(\tilde{\mathbf{v}}_h \tilde{\mathbf{v}}_h) : \nabla \tilde{\mathbf{v}}_h - \nabla \cdot (\tilde{\mathbf{v}}_h \tilde{\mathbf{v}}_h) \cdot \tilde{\mathbf{v}}_h]$	Canonical transfer of KE to window ϖ
\mathbf{Q}_P^ϖ	$\tilde{\mathbf{v}}_h \tilde{\Phi}$	Pressure flux
b^ϖ	$-\tilde{\omega} \tilde{\alpha}$	Rate of buoyancy conversion
A^ϖ	$\frac{1}{2} c (\tilde{T})^2, c = \frac{g}{T(g/c_p - L)}$	APE on window ϖ
\mathbf{Q}_A^ϖ	$\frac{1}{2} c \tilde{T} \tilde{\nabla T}$	APE flux on window ϖ
Γ_A^ϖ	$\frac{c}{2} [(\tilde{\nabla T}) \cdot \nabla \tilde{T} - \tilde{T} \tilde{\nabla} \cdot (\tilde{\nabla T})]$	Canonical transfer of APE to window ϖ
S_A^ϖ	$\frac{1}{2} \tilde{T} \tilde{\omega} \frac{\partial c}{\partial p} + \frac{1}{T} \tilde{\omega} \tilde{\alpha}$	Apparent source/sink (usually negligible)
F_A^ϖ	–	Diabatic work on window ϖ
F_K^ϖ	–	Frictional dissipation on window ϖ

a) For details, see Liang (2016)

formalism from the traditional time decomposition-based or Lorenz-type energetics formalisms, with which the law does not hold (Lorenz, 1955); see section 2 of Xu and Liang (2017) for a brief comparison. Moreover, Liang (2016) showed that the Γ terms bear a Lie bracket form, and satisfy the Jacobian identity, reminiscent of the Poisson bracket in Hamiltonian mechanics. For these reasons, such energy transfer has been termed “canonical transfer”.

The importance of canonical transfer is further revealed in its connection with the instabilities in geophysical fluid dynamics (Liang and Robinson, 2007). In particular, the transfer from the background window to the synoptic window, $\Gamma_A^{0 \rightarrow 1}$ and $\Gamma_K^{0 \rightarrow 1}$ (the superscript 0 \rightarrow 1 signifies the transfer direction), are related to the two fundamental concepts, namely, baroclinic and barotropic instabilities. For instance, a positive value of $\Gamma_A^{0 \rightarrow 1}$ ($\Gamma_K^{0 \rightarrow 1}$) indicates that the flow is baroclinically (barotropically) unstable, and the magnitude gives algebraic growth rate (note: not exponential growth rate). Figure 1 schematizes the local Lorenz cycle within the framework of a two-window decomposition. The MWT-based multiscale energetics analysis (MS-EVA) and the theory of canonical transfer have been used in a series of atmosphere-ocean researches. Recent applications include the investigations of atmospheric storm track (Zhao and Liang, 2018), atmospheric blocking (Ma and Liang, 2017), stratospheric sudden warming (Xu and Liang, 2017), tropical cyclogenesis (Wang and Liang, 2017), Kuroshio Extension variability (Yang and Liang, 2016), and eddy shedding (Zhao et al., 2016). In this study, we mainly focus on the energy cycle between the background and synoptic-scale scale windows.

3.2 Lagrangian statistical method

Also used in this study is the feature-tracking technique by Hodges (1994, 1995, 1999). This method can be used to reveal more information about storm activity (such as the storm density, intensity, geographical location, lifetime, etc.), which studies with the Eulerian method are short of. It first identifies the synoptic systems, then tracks them, and records their intensities and geographical locations at each step. In practice, the maxima of the relative vorticity (ζ) at the pressure level (e.g., 850 hPa) are chosen as the indicator of the storm center (or feature point), which forms the nodes of the storm trajectory (Hoskins and Hodges, 2002). Following previous studies, the starting time (or genesis time) is defined as the first time when ζ exceeds $1 \times 10^{-5} \text{ s}^{-1}$. In this study, we only analyze the storms whose ζ remains larger than $1 \times 10^{-5} \text{ s}^{-1}$ for at least 2 days after their genesis and that propagate more than 1000 km during their lifetime. In order to reduce the impact of the background flow on the tracking processes, the relative vorticity (ζ) is first filtered so that only

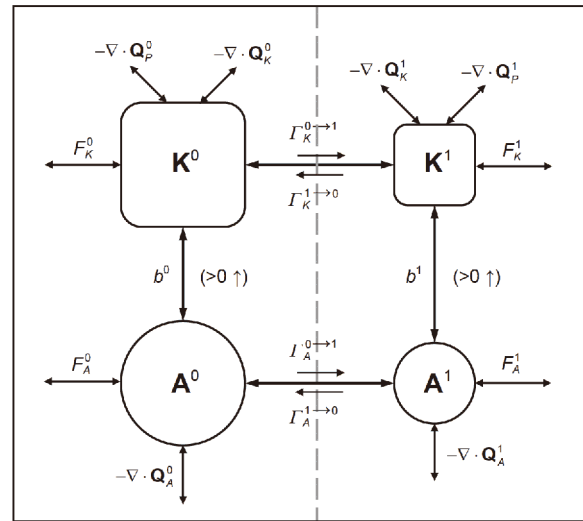


Figure 1 A schematic of the local Lorenz cycle for a two-window decomposition. The superscripts 0 and 1 stand for the scale windows. See eqs. (8) and (9) and Table 1 for interpretations of the symbols.

synoptic-scale signals are retained. In the present study, we use the synoptic fields reconstructed by the MWT to fulfill this purpose.

Based on the feature track dataset, we next compute the statistics simply through grid box counting and averaging. Two major statistics are computed, including the track density and storm intensity. We first divide the study region (i.e., the Pacific storm track in this study) into latitude-longitude grids, each with a side length of 5° . That is to say, each grid is equivalent to a 5° spherical cap. Second, if a storm enters or passes through a grid, the track density of that grid increases by one. The raw density statistics are subsequently scaled to number densities per month (30 days) for analysis and display. The storm intensity of one grid is simply defined as the mean strength of the relative vorticity of all the feature points once within it.

4. Results and discussions

4.1 Seasonal variation of transient energy

To see the seasonal variation of the Pacific storm-track strength, in Figure 2 we display the latitude-time distributions of the vertically (1000–100 hPa) integrated and zonally averaged transient (or synoptic) available potential energy (TAPE) and kinetic energy (TKE) over the storm-track region (120°E–120°W). These distributions reflect the variations in intensity and meridional location (The result is the climatologically daily evolution from September 1957 to June 2002. There are only 11 records on February 29, but whether dropping or retaining this day has no impact on the final result). We see that the intensities of TAPE (Figure 2a) and TKE (Figure 2b) change significantly with time. Both

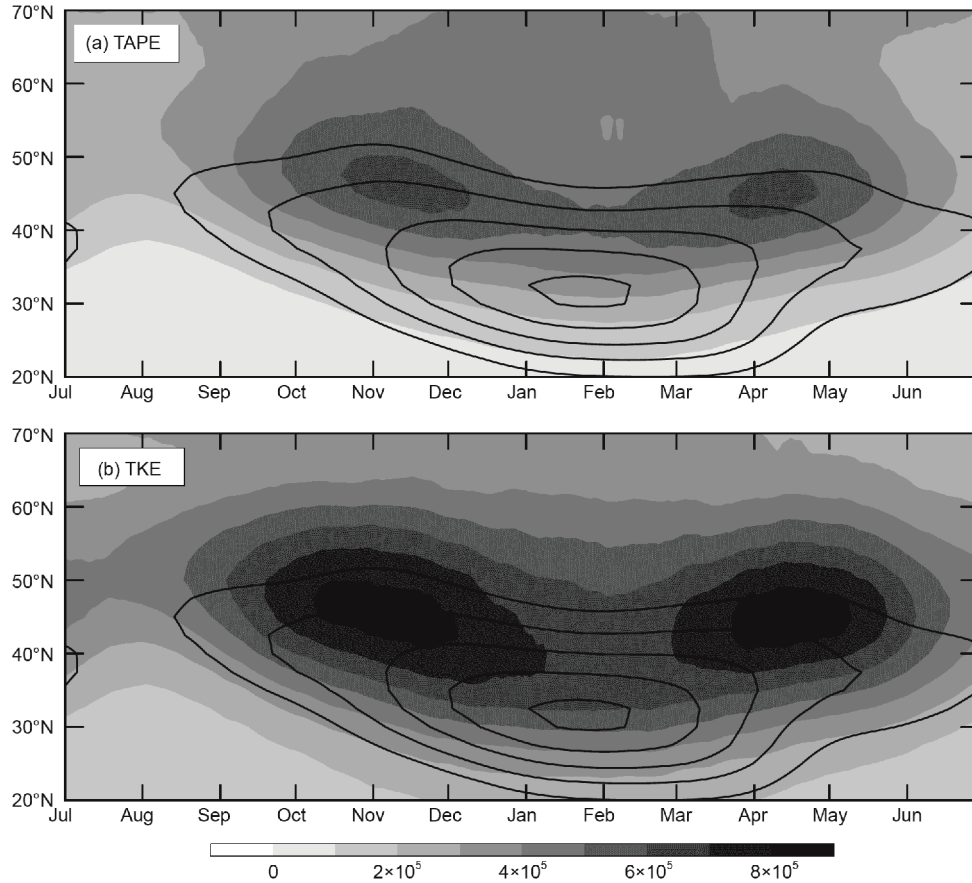


Figure 2 Latitude-time distributions (climatology, 1957–2002) of the vertically (1000–100 hPa) integrated (upper) transient available potential energy (unit: $\text{m}^2 \text{s}^{-2}$) and (lower) transient kinetic energy (unit: $\text{m}^2 \text{s}^{-2}$). The transient energy has been averaged over the longitude band 120°E – 120°W . The black contours denote the 300-hPa zonal wind, starting from 10 m s^{-1} with an interval of 10 m s^{-1} . The zonal wind has been averaged over the longitude band 120°E – 180° .

peak in late fall (November) and early spring (April), leaving a minimum in midwinter (January–February) when the jet is the strongest throughout the year. The two peaks in magnitude are generally symmetrically distributed about the minimum in midwinter. Quantitative calculation shows that TAPE and TKE are about 20% (calculated as the difference between seasons divided by the value of late fall/early spring) weaker in midwinter than in late fall/early spring. Figure 2 also shows the latitude-time distribution of the 300-hPa zonal wind. We see that the center of the storm track is located about 10 latitudes north of the jet center. Both jet and storm track migrate northward and southward with time, reaching their respective southernmost points in midwinter (near 30°N and 40°N respectively), and then gradually move northward toward the northernmost points (around 40°N and 50°N) in summer. According to the theory of linear baroclinic instability (Eady, 1949; Lindzen and Farrell, 1980), the intensity of storm activity should be proportional to the vertical shear of the jet wind. That is to say, the storm track should attain its peak intensity in midwinter. Here it, however is obviously not the case. In the following, we analyze the physical processes represented by the right-hand side of

eqs. (8) and (9), to seek for the causes of the storm activity, which appears weaker in midwinter than in either fall or spring.

4.2 Energy transfer and conversion

Energy transfers reflect the interaction between the synoptic and background scale windows. They in conjunction with buoyancy conversion can reveal the internal dynamics within a fluid flow. Figure 3 shows the latitude-time evolution of the baroclinic canonical transfer ($\Gamma_A^{0 \rightarrow 1}$) and buoyancy conversion (b^1), where results have been vertically integrated and zonally averaged over the entire Pacific storm-track region, same as Figure 2. (Unless otherwise stated, the latitude-time evolution maps of the other quantities are same.) Baroclinic canonical transfer corresponds to baroclinic instability, with positive values indicating instability and negative values stability. One can see that $\Gamma_A^{0 \rightarrow 1}$ is positive in almost the entire domain (Figure 3a), implying that the system is baroclinically unstable, with APE transfer from the background window to the synoptic window to increase TAPE. This re-

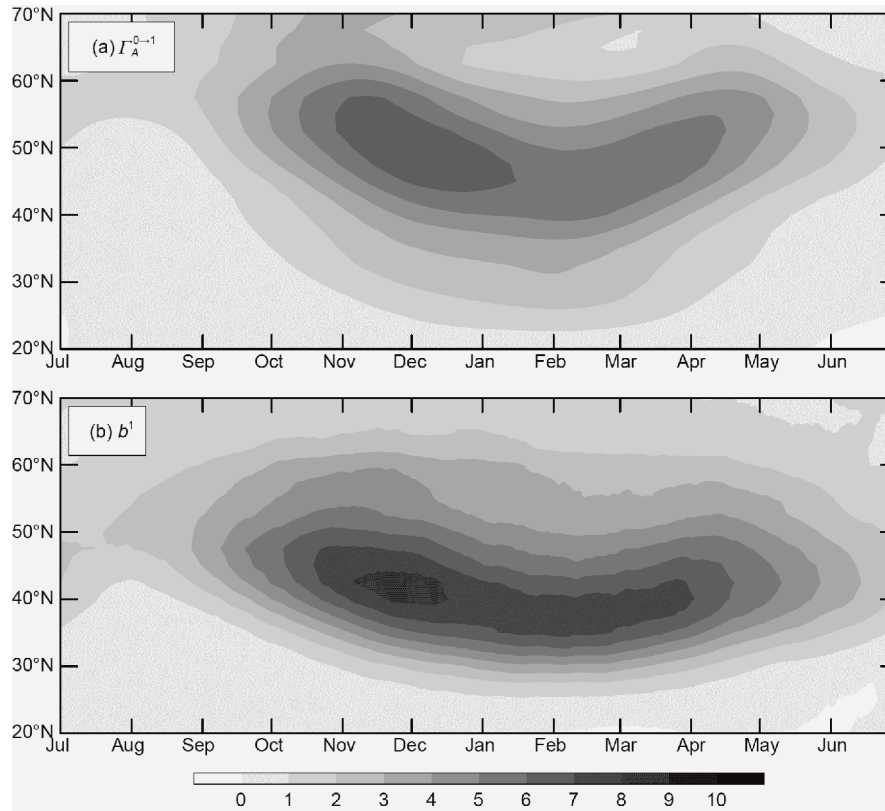


Figure 3 Same as Figure 2, but for (a) baroclinic canonical transfer (unit: $\text{m}^2 \text{s}^{-3}$) and (b) buoyancy conversion (unit: $\text{m}^2 \text{s}^{-3}$).

confirms the importance of baroclinic instability as an important source of energy for mid-latitude storm tracks (Simmons and Hoskins, 1978; Pierrehumbert and Swanson, 1995; Chang et al., 2002). Seasonally the $I_A^{0 \rightarrow 1}$ center also migrates in the north-south direction. It is generally parallel to the TAPE center (Figure 2a) and is located 5–10 latitudes farther north. However, unlike TAPE, the evolution of $I_A^{0 \rightarrow 1}$ is asymmetric about midwinter. Throughout the year, $I_A^{0 \rightarrow 1}$ has only one peak in late fall and early winter (Figure 3a). After that, it gradually weakens with time and becomes weakest in summer. Buoyancy conversion (b^1) is also positive in the domain (Figure 3b), indicating that the conversion is from TAPE to TKE. The central latitude of b^1 roughly coincides with that of the storm track, migrating in the north-south direction as time goes on. Similar to $I_A^{0 \rightarrow 1}$, b^1 is also seasonally asymmetric. It is maximized in late fall and early winter, and then weakens over time. Chen et al. (2013) found that baroclinic transfer (in the traditional sense) is weaker in midwinter than in fall and spring, and hence he believed that it makes a direct cause for the formation of MWM. Here, $I_A^{0 \rightarrow 1}$ is also found to play an important role, but it is asymmetric in the seasonal evolution, and its contribution is only seen in fall; in spring its role is the opposite— $I_A^{0 \rightarrow 1}$ is actually weaker then.

The latitudinal-time evolution of barotropic canonical transfer ($I_K^{0 \rightarrow 1}$) is shown in Figure 4. One can see that $I_K^{0 \rightarrow 1}$ is negative in almost the whole domain except for the subtropical region (around 30°N) in winter with a small positive value, indicating that the background flow over the Pacific storm-track region is generally barotropically stable, with KE transferring from the eddy field to the background flow, hence reducing TKE. The latitude-time evolution of $I_K^{0 \rightarrow 1}$ is consistent with that of TKE, with three extrema appearing respectively in November, April, and midwinter. Note that both the November and April extrema are stronger than the midwinter one. Since $I_K^{0 \rightarrow 1}$ here is consuming TKE, it plays an opposite role in the formation of MWM, consistent with previous results based on traditional methods (Chang, 2001; Yin, 2002; Harnik and Chang, 2004; Chang and Zurita-Gotor, 2007; Chen et al., 2013).

4.3 Non-local processes

Non-local processes are represented by energy flux convergence terms in the energetic balance. Figure 5 shows the latitude-time distributions of the flux convergences of energy and geopotential. We see that the TAPE flux convergence ($-\nabla \cdot \mathbf{Q}_A^1$) is mainly negative (positive) north (south) of 45°N, indicating that the TAPE flux is divergent in the north and

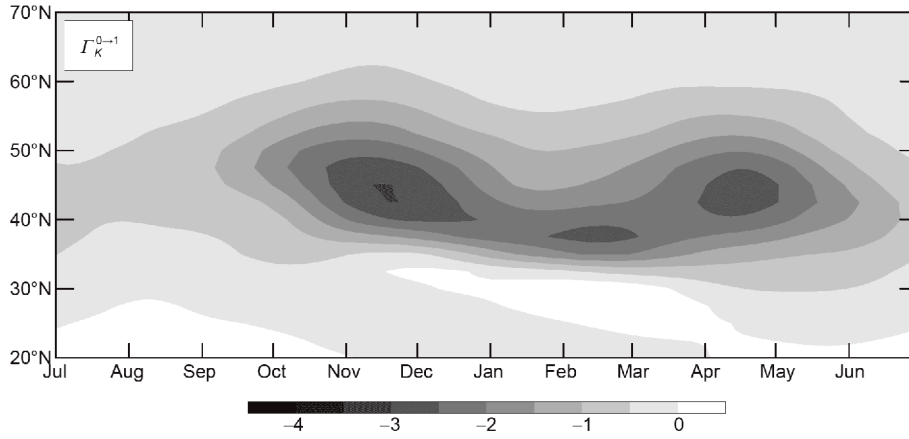


Figure 4 Same as Figure 3, but for barotropic canonical transfer (unit: $\text{m}^2 \text{s}^{-3}$).

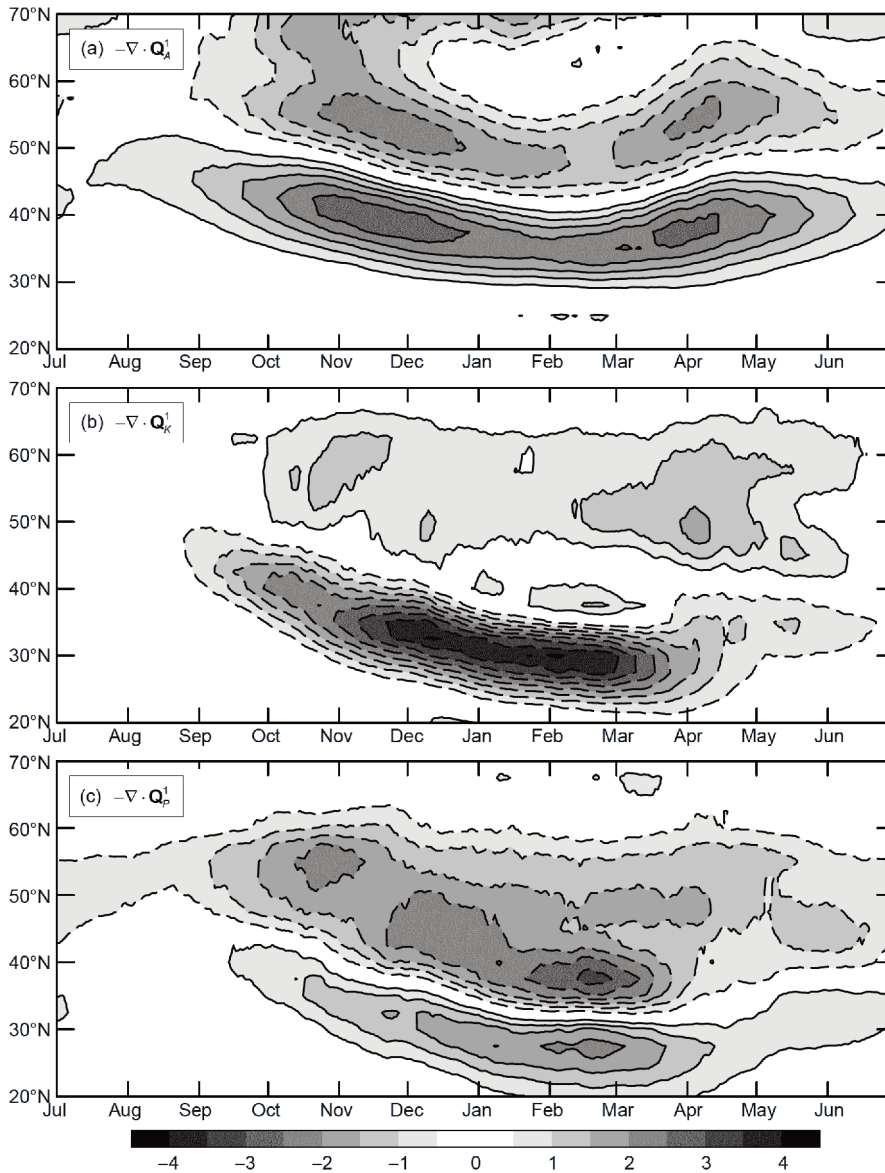


Figure 5 Same as Figure 3, but for (a) the convergence of TAPE flux (unit: $\text{m}^2 \text{s}^{-3}$), (b) the convergence of TKE flux (unit: $\text{m}^2 \text{s}^{-3}$), and (c) the convergence of geopotential flux (unit: $\text{m}^2 \text{s}^{-3}$). Negative contours are indicated with dashed lines (zero contour omitted).

convergent in the south, which explains why the TAPE center is located on the southern side of the $\Gamma_A^{0 \rightarrow 1}$ center (see Figures 2a and 3a). Moreover, the convergence (divergence) is strong in November and April, and is comparably weak in winter. Similarly, the TKE flux convergence ($-\nabla \cdot \mathbf{Q}_K^1$) is negative (positive) south (north) of 40°N . The negative center in the south is strong (especially in winter), whereas the positive center in the north is weak (mainly appears in November and especially April). For the geopotential flux convergence ($-\nabla \cdot \mathbf{Q}_P^1$), it is positive (negative) south (north) of 40°N . Both the convergence and the divergence in the south and north respectively reach their maxima in winter. From above, the energy and geopotential flux convergences all have notable seasonal variations, and their roles in the formation of MWM depend on which convergence/divergence dominates the domain. In the following we will clarify this in our calculations.

4.4 External forcing

External forcing mainly includes diabatic processes and frictional dissipation, both playing important roles in balancing the atmospheric energy budget. In this study, they are calculated as the residues of eqs. (8) and (9). Figure 6 shows

the latitude-time distributions of diabatic work (F_A^1) and frictional dissipation (F_K^1). It can be seen that F_A^1 is positive in almost the whole domain (Figure 6a), indicating that F_A^1 functions as a source of TAPE. Temporally F_A^1 has seasonal variation. It is strong in late fall and early spring, and is weak in midwinter. In contrast, F_K^1 is negative throughout the domain (Figure 6b); that is to say, it makes a major TKE sink. Different from F_A^1 , there are two bands of negative values for F_K^1 , which are located near 40°N and 60°N . F_K^1 also varies from season to season; it is strongest in late fall and early winter, and is weak in spring. These results indicate both diabatic processes and frictional dissipation contribute to the formation of MWM. Diabatic processes are beneficial to the relative increase of TAPE in spring and fall, whereas the reduced frictional dissipation in spring contributes to the TKE maintenance.

To further understand the seasonal energetics variation and its role in the formation of MWM, Figure 7 shows the evolutions of the energetics processes averaged over the entire Pacific storm-track area. One can see that baroclinic canonical transfer, diabatic work, and buoyancy conversion attain their respective maxima in late fall (Figure 7a), and then weakened over time (note the diabatic work also slightly re-

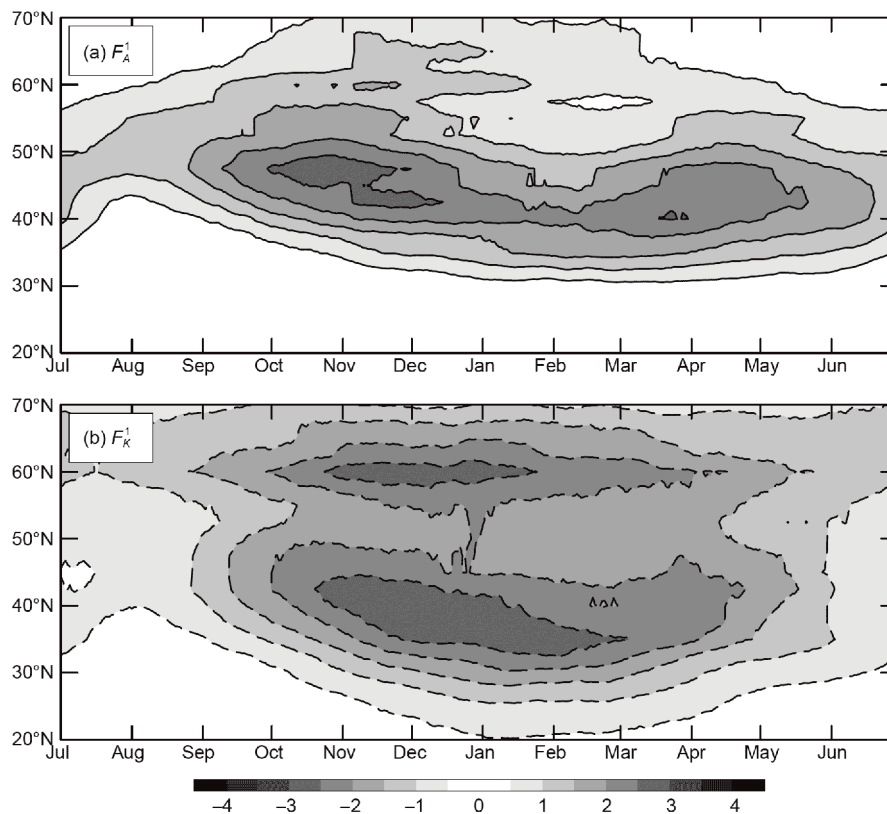


Figure 6 Same as Figure 3, but for contributions from (a) diabatic effect (unit: $\text{m}^2 \text{s}^{-3}$) and (b) frictional dissipation (unit: $\text{m}^2 \text{s}^{-3}$). Negative contours are indicated with dashed lines (zero contour omitted).

inforces in early spring); frictional dissipation is strong in fall and winter (strongest in midwinter), but weak in spring; energy and geopotential flux convergences are negative in fall and winter (Figure 7b), indicating a net outflow of eddy energy in the Pacific storm-track region, whereas in spring it turns into a positive value—a net inflow of eddy energy. In short, we see that the MWM is not determined by a single factor, but by multiple factors. Moreover, the energy processes behind the MWM show seasonal asymmetry. In late fall, baroclinic canonical transfer, buoyancy conversion and diabatic work are abnormally strengthened, leading to a storm track stronger in fall than that in winter. In early spring, in contrast, the strengthening of the storm track is primarily due to the enhancement of the eddy energy fluxes and the weakening of frictional dissipation.

4.5 An energy budget analysis

To clarify the relative importance of the energetics processes in the MWM formation, this section provides a quantitative discussion of the contribution of each process. Because both TAPE and TKE peak in November and April, and the suppression occurs in January-February (see Figure 2), we only analyze these four months. November is used to stand for late fall, April for early spring, and January-February for midwinter. For convenience, terms at the right hand side of eqs. (8) and (9) are integrated over the entire Pacific storm-track

domain (1000–100 hPa, 20°N–70°N, 120°E–120°W)

$$\langle A \rangle = - \int_{\lambda} \int_{\phi} \int_p \frac{Aa^2}{g} \cos\phi d\phi d\lambda dp, \quad (11)$$

where A is any field, a , ϕ and λ are the earth's radius, latitude and longitude respectively. Figure 8 shows the energy balance of the three periods, and the differences between late fall/early spring and midwinter. Generally, baroclinic canonical transfer and diabatic work are two main sources of TAPE, accounting for 73% and 27% of the total source, respectively. Buoyancy conversion simultaneously plays the roles of the TAPE main sink, and main source of TKE. For TKE, the main sinks include barotropic canonical transfer and frictional dissipation, which respectively account for 26% and 49% of the total sink. Besides, the TKE flux divergence and the geopotential flux divergence are also TKE sinks.

In this study, we mainly concern ourselves with the relative changes in the contribution of each energy process to the energy budget. Figure 8d shows the difference of the energy budget between midwinter and late fall. It can be seen that the most significant difference lies in diabatic work and barotropic canonical transfer. Diabatic work in midwinter is 30% (the difference divided by the late-fall value) weaker than that in late fall, which is conducive to the formation of MWM. Upscale KE transfer in midwinter is about 39% weaker than that in late fall, which is not beneficial to the

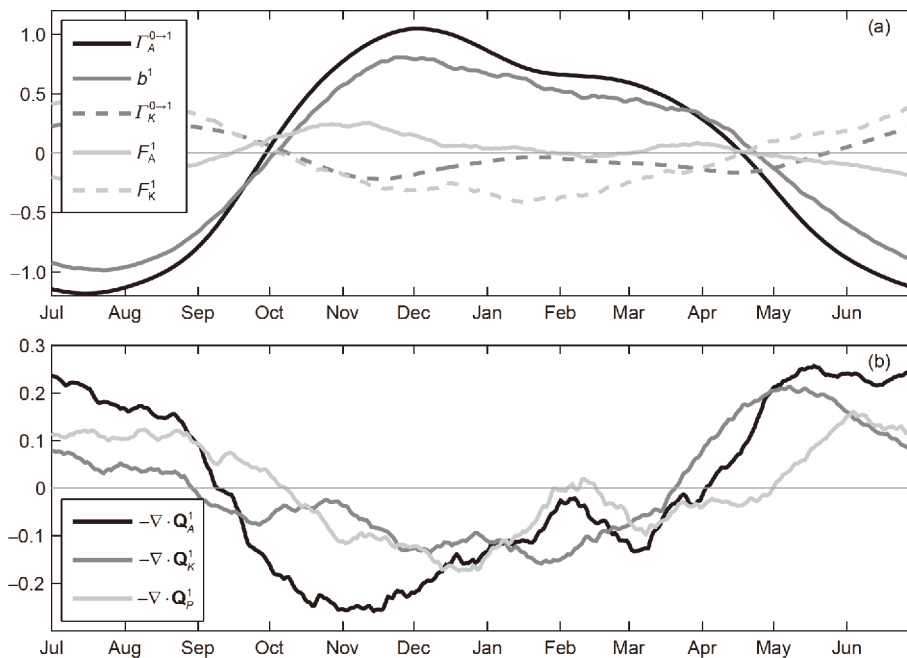


Figure 7 Seasonal variation of the volume-averaged energetics: (a) baroclinic canonical transfer (Γ_A^{0-1}), barotropic canonical transfer (Γ_K^{0-1}), buoyancy conversion (b^1), diabatic effect (F_A^1), and frictional dissipation (F_K^1); (b) the TAPE flux convergence ($-\nabla \cdot \mathbf{Q}_A^1$), the TKE flux convergence ($-\nabla \cdot \mathbf{Q}_K^1$), and the geopotential flux convergence ($-\nabla \cdot \mathbf{Q}_p^1$). Unit: $\text{kg m}^2 \text{s}^{-3}$. The results have been vertically integrated and horizontally averaged in the Pacific storm-track domain (20°N–70°N; 120°E–120°W; 1000–100 hPa), where the annual mean has been removed.

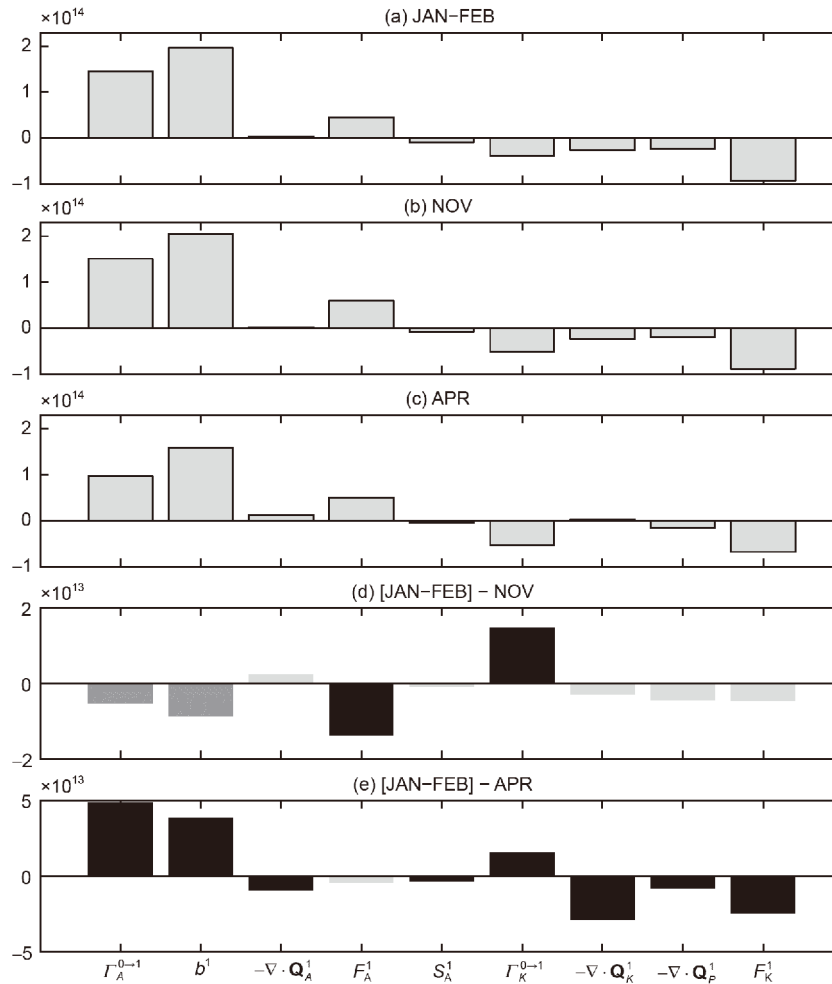


Figure 8 Energy budgets for the three seasons: (a) January–February, (b) November and (c) April. The difference between (d) January–February and November, and (e) January–February and April. All quantities have been integrated over the Pacific storm-track domain (20°N – 70°N , 120°E – 120°W) between 1000 and 100 hPa. Unit: $\text{kg m}^2 \text{s}^{-3}$. The bars in black ((d) and (e)) denote the statistically significant quantities by the two-sided t -test at the 0.01 level, and the bars in dark gray (in d) denote those at the 0.1 level.

formation of MWM. In addition, baroclinic canonical transfer and buoyancy conversion are both weaker in midwinter than in late fall, which is beneficial to MWM. In general, as compared to the late fall, the reduction of baroclinic canonical transfer and diabatic work in midwinter are the direct causes of the relatively weak storm track in midwinter.

Figure 8e shows the difference of the energy budget between midwinter and early spring. Excluding diabatic work, it is evident that significant differences exist in all energy processes. The most obvious differences lie in baroclinic canonical transfer and buoyancy conversion. They are two major sources of TAPE and TKE, and are 33% and 20% stronger in midwinter than in early spring. Based on this one would expect that the eddy energy in midwinter should be more than that in spring. However, it is obviously the opposite. This is because the energy flux divergence and frictional dissipation as two main sinks of eddy energy are

much stronger in midwinter than in spring, making the eddy energy dissipate rather rapidly in midwinter. Specifically, TAPE flux convergence in early spring is nearly four times that of midwinter. The TKE flux is divergent in midwinter, and convergent in spring. The geopotential flux is divergent in midwinter, and is 33% larger than that in early spring. In addition, the frictional dissipation in spring is 26% weaker than in midwinter. Among the above differences, the largest part comes from the TKE flux convergence and frictional dissipation. To further seek for the cause, the three components (x -, y -, and z -direction) of the TKE flux convergence are separately analyzed. It is found that the largest contribution comes from the x -component. Figure 9 shows the overall eastward energy fluxes through the vertical meridional sections (20°N – 70°N , 1000–100 hPa) along 120°E (the storm-track entrance) and 120°W (the exit) in spring and midwinter and the difference between the two sections. We see that TAPE and TKE entering the storm

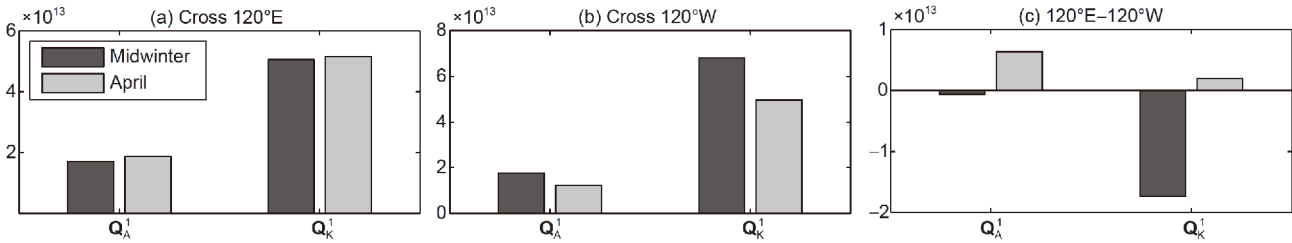


Figure 9 Transient energy fluxes (unit: $\text{m}^3 \text{s}^{-3}$) through (a) 120°E and (b) 120°W . A positive value means directing eastward. (c) The difference between (a) and (b), with positive value standing for net energy increase. All quantities have been integrated over (20°N – 70°N , 100 – 1000 hPa) in each meridional section.

track through the 120°E section is less in midwinter whereas that flowing out through 120°W are more. Therefore, the net inflow of eddy energy into the storm track is larger in spring than in winter.

5. Further discussion on the physical causes of the midwinter suppression

We have so far identified the direct causes of MWM via the energy budget. Some issues still exist. For example, why is the baroclinic canonical transfer stronger in fall than in winter although the fall-time jet wind is weaker? Although spring-time baroclinic canonical transfer is weaker than in winter, why is storm activity nonetheless stronger? In the following subsections, we look for clues from the spatial distributions of the energy processes.

5.1 Why is the baroclinic canonical transfer stronger in fall than in winter?

Figure 10 shows the distributions of the vertically integrated TAPE and TKE in the North Pacific. Both are significantly weaker in midwinter (Figure 10a and 10b) than in spring and fall (Figure 10c–10f). Compared to late fall and early spring, TAPE in midwinter is weakened (enhanced) north (south) of 40°N . Moreover, the decrease in the north is more significant than the increase in the south (Figure 10c and 10e). TKE also has similar seasonal variation (Figure 10d and 10f). Overall, the Pacific Storm track is weaker in winter than in spring and fall.

Baroclinic canonical transfer and buoyancy conversion are two important sources of eddy energy. Figure 11 shows the distributions of the vertically integrated $\Gamma_A^{0 \rightarrow 1}$ and b^1 and their differences between seasons. It can be seen that $\Gamma_A^{0 \rightarrow 1}$ is mainly concentrated over the East Asia–Western Pacific region. It is strong in winter (Figure 11a) and fall (Figure 11b), and weak in spring (Figure 11c). Its difference between winter and spring/fall (Figure 11b and 11c) is similar to that of TAPE (Figure 10), with positive (negative) anomaly in the south (north). That is, compared to spring and fall, $\Gamma_A^{0 \rightarrow 1}$ in

winter is weakened in the middle and high latitudes, whereas enhanced in the subtropical region. b^1 has similar seasonal variation (Figure 11d–11f). However, the distributions of the difference between winter and fall, and that between winter and spring are different. For the former, the northern negative center is stronger than the southern positive center (Figure 11b and 11e), whereas it is reversed in the latter (Figure 11c and 11f). In addition, the centers of $\Gamma_A^{0 \rightarrow 1}$ (Figure 11c) and b^1 (Figure 11f) shift to the East Asia region in spring.

Eddy energy is largely determined by baroclinic canonical transfer and the buoyancy conversion, while the former is directly related to the background flow. Figure 12 shows the distribution of the 300-hPa zonal wind. One notable feature is the seasonal variation of its strength. The wind is strongest in winter, with more than 60 m s^{-1} at the center; then in fall, with 40 m s^{-1} at the center. It is weakest in spring, with only 30 m s^{-1} at the center. In addition, the jet in midwinter is basically zonally distributed and located southward (the jet core is near 32.5°N ; Figure 12a). Although the jet-core location at its entrance in spring and fall is similar to that in winter, the two jets tilt northeastward, making the jet center located to the north of 40°N in the central and eastern Pacific (Figure 12b and 12c). Therefore, the difference in the zonal wind between winter and spring (fall) shows a dipole distribution with positive (negative) anomaly south (north) of 40°N , similar to the distribution of the difference in eddy energy (Figure 10) and $\Gamma_A^{0 \rightarrow 1}$ (Figure 11). This shows that, when taking the spatial distribution into consideration, the MWM does not contradict the traditional linear baroclinic instability theory (Charney, 1947; Eady, 1949; Lindzen and Farrell, 1980)—The area with relatively strong zonal wind has relatively large baroclinic canonical transfer and eddy energy. But there is still an issue that needs further clarification. Compared with late fall, in winter the strengthening of the zonal wind south of 40°N (over 30 m s^{-1}) is significantly greater than the weakening in the northern region (about 15 m s^{-1} ; Figure 12b). However, the corresponding decrease in baroclinic canonical transfer (Figure 11b) and eddy energy (Figure 10c and 10d) in the south is significantly less than the increase in the north. The answer to this question is also the key to understanding why the baroclinic ca-

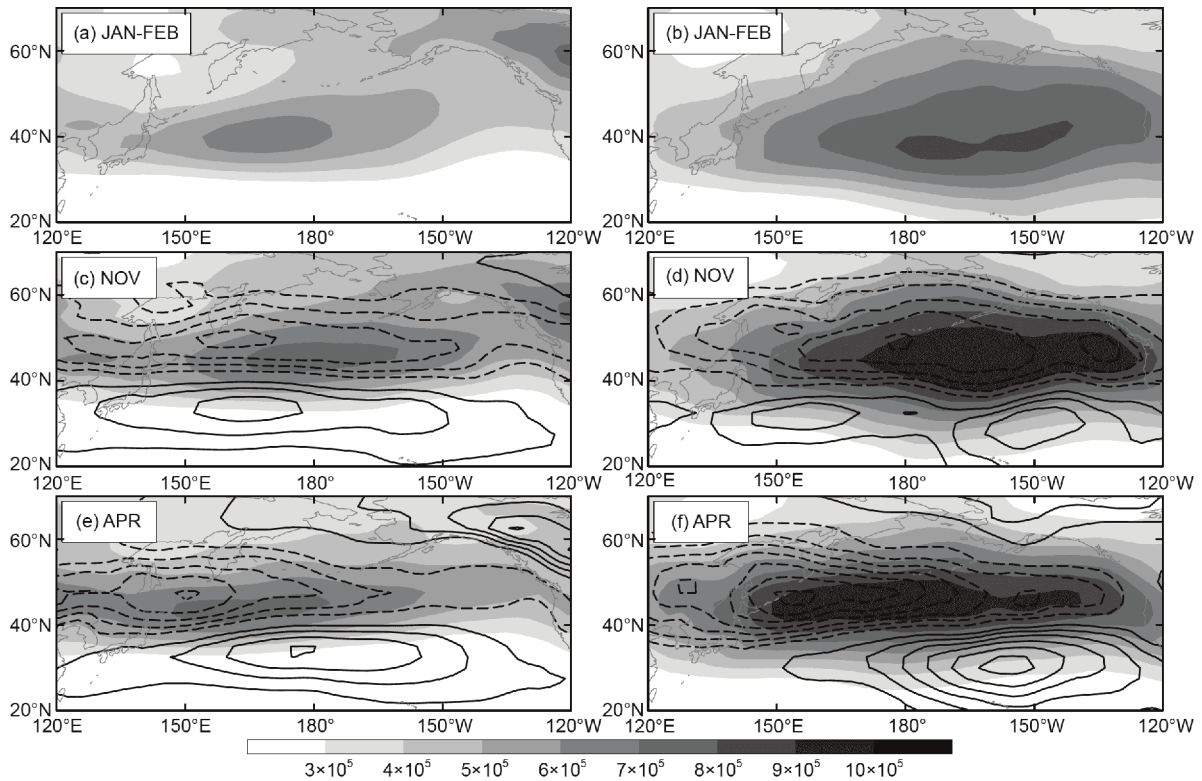


Figure 10 (Left column) Distributions of vertically integrated TPE (unit: $\text{m}^2 \text{s}^{-2}$) and (right column) TKE (unit: $\text{m}^2 \text{s}^{-2}$): ((a)–(b)) midwinter, ((c)–(d)) late fall, ((e)–(f)) early spring, where the vertical integration is performed between 1000 and 100 hPa. The black contours in (c)–(f) indicate the difference between midwinter and the corresponding month. The contour interval is $5 \times 10^4 \text{ m}^2 \text{s}^{-2}$. Negative contours are indicated with dashed lines (zero contour omitted).

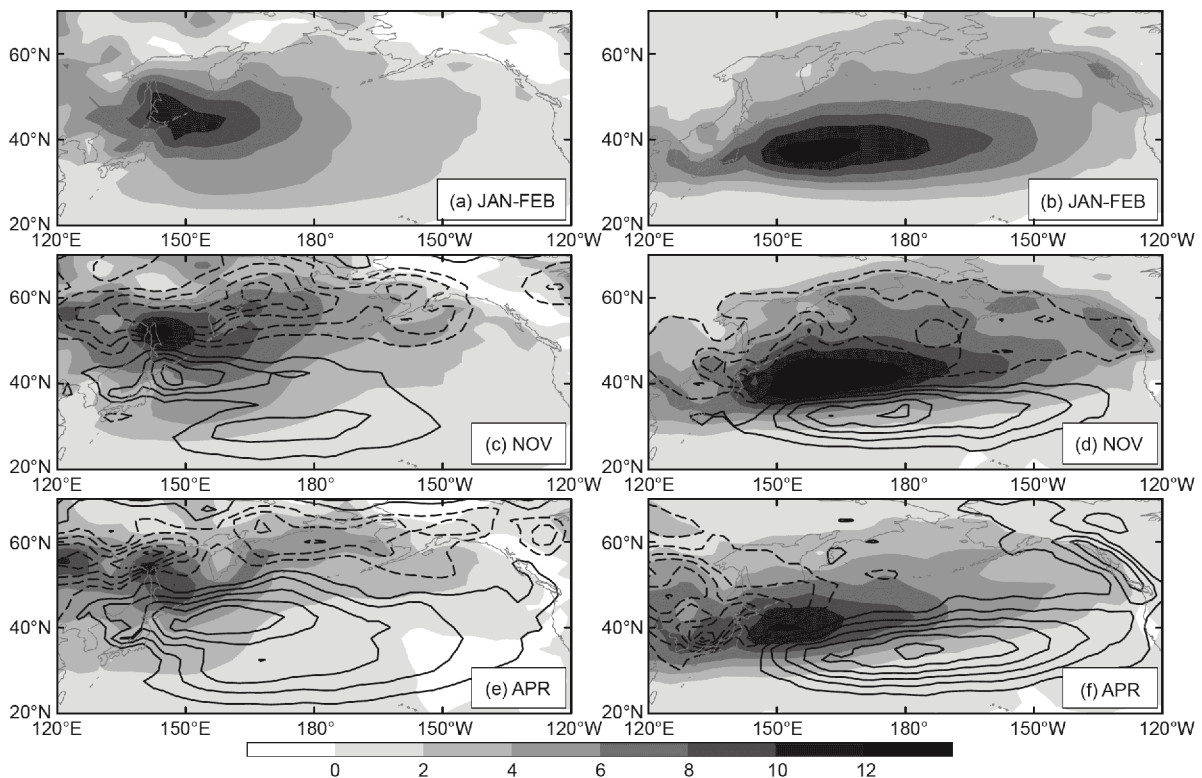


Figure 11 Same as Figure 10, but here is the (left column) baroclinic canonical transfer (unit: $\text{m}^2 \text{s}^{-3}$) and (right column) buoyancy conversion (unit: $\text{m}^2 \text{s}^{-3}$), with an interval of $1 \text{ m}^2 \text{s}^{-3}$. Negative contours are indicated with dashed lines (zero contour omitted).

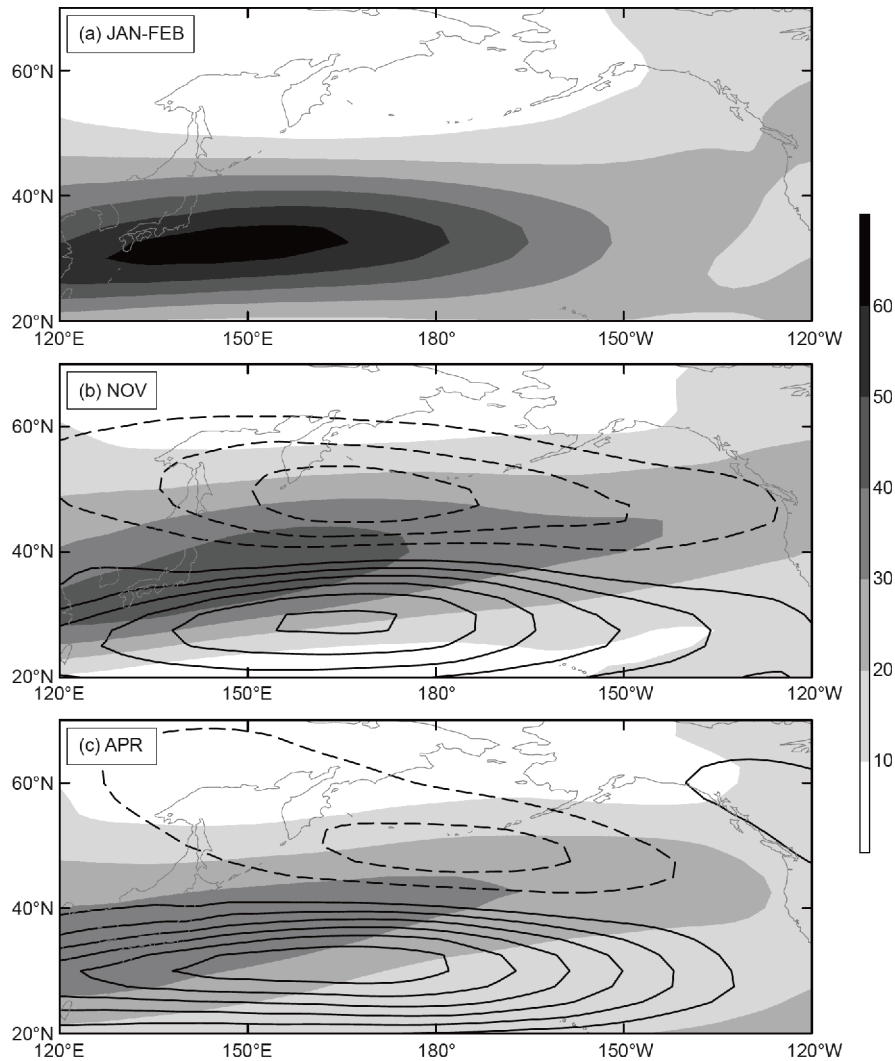


Figure 12 Horizontal distribution of the climatologically mean 300-hPa zonal wind: (a) midwinter, (b) late fall, and (c) early spring. The black contours indicate the difference between midwinter and the corresponding month. The contour interval is 5 m s^{-1} . Negative contours are indicated with dashed lines (zero contour omitted).

nonical transfer is weaker in winter than in fall even if the wind is stronger in winter.

Here, we use the Lagrangian statistical method together with the results of the energetics diagnosis to explain why the baroclinic canonical transfer is suppressed in winter. We first use a feature-tracking technique (Hodges, 1994, 1995, 1999) to obtain the trajectory (or track) density of the synoptic storms within the Pacific Storm track. For the specific procedures, please refer to section 3.2. Figure 13 shows the geographical distribution of the monthly mean storm trajectory density on the 850-hPa isobaric surface. One can see that, different from the storm-track center obtained above via the energetics method which shows obvious seasonal north-south migration (see Figure 2), the central latitude of the storm trajectory density is relatively fixed. The trajectory center is located near 45°N to the east of Japan in all three seasons, consistent with previous studies (Chung et al., 1976;

Chen et al., 1991; Chang, 1993; Wang and Rogers, 2001; Hoskins and Hodges, 2002) (If the mid-latitude storms are mainly generated from baroclinic instability, then the center of the storm trajectory is expected to coincide with the center of the jet stream (and thus moves north-south with seasons) since the jet stream center is most unstable. However, the statistical results show that the center position of the storm trajectory rarely changes with season, demonstrating that the storms in the mid-latitudes are mostly generated via other mechanisms (such as topographic forcing, thermal forcing, energy dispersion, etc.), i.e., Type-B cyclones (Petterssen and Smebye, 1971; Farrell, 1984)). The jet stream has significant north-south movements with time, arriving at its southmost position in midwinter, whereas the storm-track center is relatively fixed and mainly located in middle and high latitudes. This makes the jet center and the storm-track center far apart in winter (Figure 13a), which is not beneficial

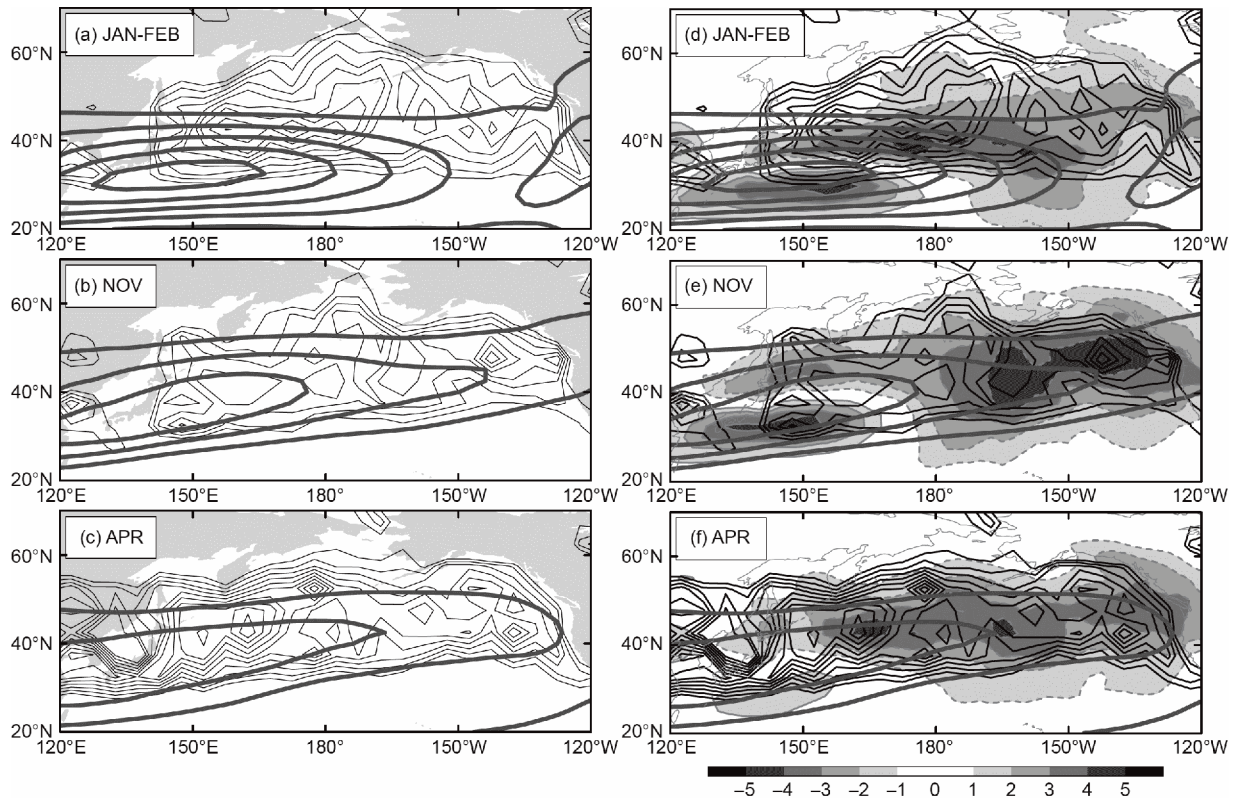


Figure 13 (Left column) The horizontal distribution of the storm track density (thin contours with an interval of 0.2 (per 5° spherical cap), starting from 0.8 (per 5° spherical cap)) at the 850-hPa level. Overlaid is the 300-hPa zonal wind (thick contours with an interval of 10 m s^{-1} , starting from 20 m s^{-1}). (Right column) Same as the left column, but the colors indicate the vertically integrated barotropic canonical transfer ($\text{m}^2 \text{ s}^{-3}$). Negative contours are indicated with dashed lines (zero contour omitted).

to storm-jet interactions. The energy obtained by storms from the background field is therefore reduced, and storm activity weakened. Since the storm is mainly located in the middle and high latitudes, the weakening of eddy activity is thus most significant there (refer to Figure 10c–10f). Although the jet wind in the subtropical region is significantly enhanced in winter, its actual impact on the storm activity is minor due to the distance from the northern storms. Therefore, the storm track is overall weakened in winter. Conversely, in spring and fall (Figure 13b and 13c), jet and storm trajectory centers almost coincide (especially in the central and eastern Pacific). Therefore, the eddy-background flow interaction is strong, and the storm activity is also strong (Although the jet center and the storm-track center overlap substantially in spring, it does not produce strong baroclinic canonical transfer since the jet in spring is too weak). In fact, the relative positional relation between the storm-track and jet centers has also an obvious influence on barotropic canonical transfer. As shown in Figure 13d–13f, upscale KE transfer is strong in the area where the jet and storm trajectory overlap, and weak elsewhere. In winter, the overlapping region between the two is limited, and the upscale KE transfer is also weak (Figure 13d), weakening the MWM.

In short, the intensity of the canonical energy transfer

depends not only on the intensities of the storm and the jet, but also on the positional relation between them. In winter, the jet is located southward, far from the storms. The interaction between them is thus suppressed, and the downscale APE and upscale KE transfers are weakened. This is why the jet stream is strongest in midwinter but the canonical energy transfer is weaker than that in spring and fall (Note the baroclinic canonical transfer in spring is actually weaker than in winter; see the explanation in the footnote).

5.2 Why is storm activity stronger in spring than in winter although the spring-time baroclinic canonical transfer is weaker?

It can also be seen from Figure 13 that the storm trajectory density in spring is significantly greater than that of winter, especially at the entrance of the storm track, suggesting the effect of upstream seeding is stronger in spring. Figure 14 shows the meridional section distributions of the zonal-mean storm trajectory density and storm intensity at the entrance of the storm track (120°E – 140°E). One can see that both the track density and storm intensity are greater in spring and fall than in winter. For instance, in spring the track density is over 1.3 and the intensity is over $8 \times 10^{-5} \text{ s}^{-1}$, whereas in winter

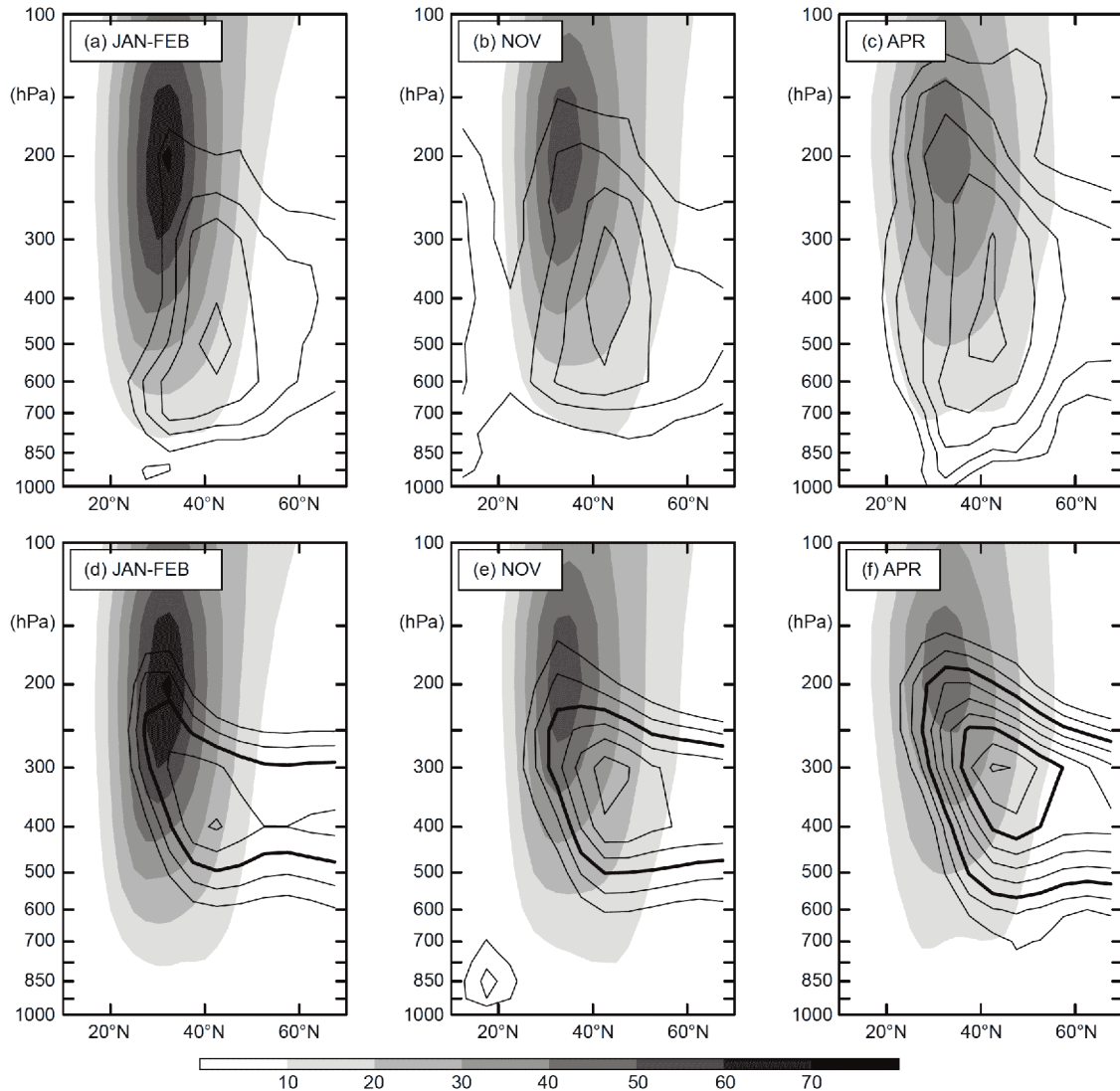


Figure 14 Vertical-longitudinal distributions of ((a)–(c)) storm track density (thin black line, with an interval of 0.2, starting from 0.8) and ((d)–(f)) storm intensity (thin black line, with an interval of $5 \times 10^{-4} \text{ s}^{-1}$, starting from $4 \times 10^{-5} \text{ s}^{-1}$). The thick lines in storm intensity indicate the isolines of $5 \times 10^{-3} \text{ s}^{-1}$ and $7 \times 10^{-3} \text{ s}^{-1}$, respectively. Overlaid is the zonal wind (shaded, m s^{-1}).

they are 1.1 and $6 \times 10^{-5} \text{ s}^{-1}$, respectively. This demonstrates that the disturbance source upstream of the Pacific is strong in spring. The number (intensity) of storms from the upstream into the North Pacific area is larger (stronger) in spring than in winter, in agreement with the conclusions in Section 4.5, that is, more eddy energy are fluxed into the storm track from its entrance in spring (refer to Figure 9). Therefore, non-local processes play a vital role in the storm-track strength in spring, consistent with the upstream seeding mechanism proposed by Penny et al. (2010, 2011, 2013). As regards why the frequency (intensity) of the storm at the entrance reaches the highest (strongest) in spring, further investigations are required. Briefly, we hypothesized that this may be related to the diabatic work in the storm track entrance area. As shown in Figure 15, diabatic work in the spring is extremely strong at the storm-track entrance (Figure

15c), which generates more APE for storms to grow. In addition, frictional dissipation in spring is significantly reduced almost over the entire North Pacific (Figure 15f), which favors strong storms from the upstream into the Pacific to be maintained for a long time even in the absence of strong baroclinicity.

6. Conclusions

By the theory of linear baroclinic instability, the mid-latitude atmospheric storm track should attain its maximum intensity in winter when the baroclinicity of the atmosphere is the strongest in the year. However, unexpectedly, the Pacific storm track is stronger in late fall and early spring than in midwinter. Historically, this phenomenon has been called the

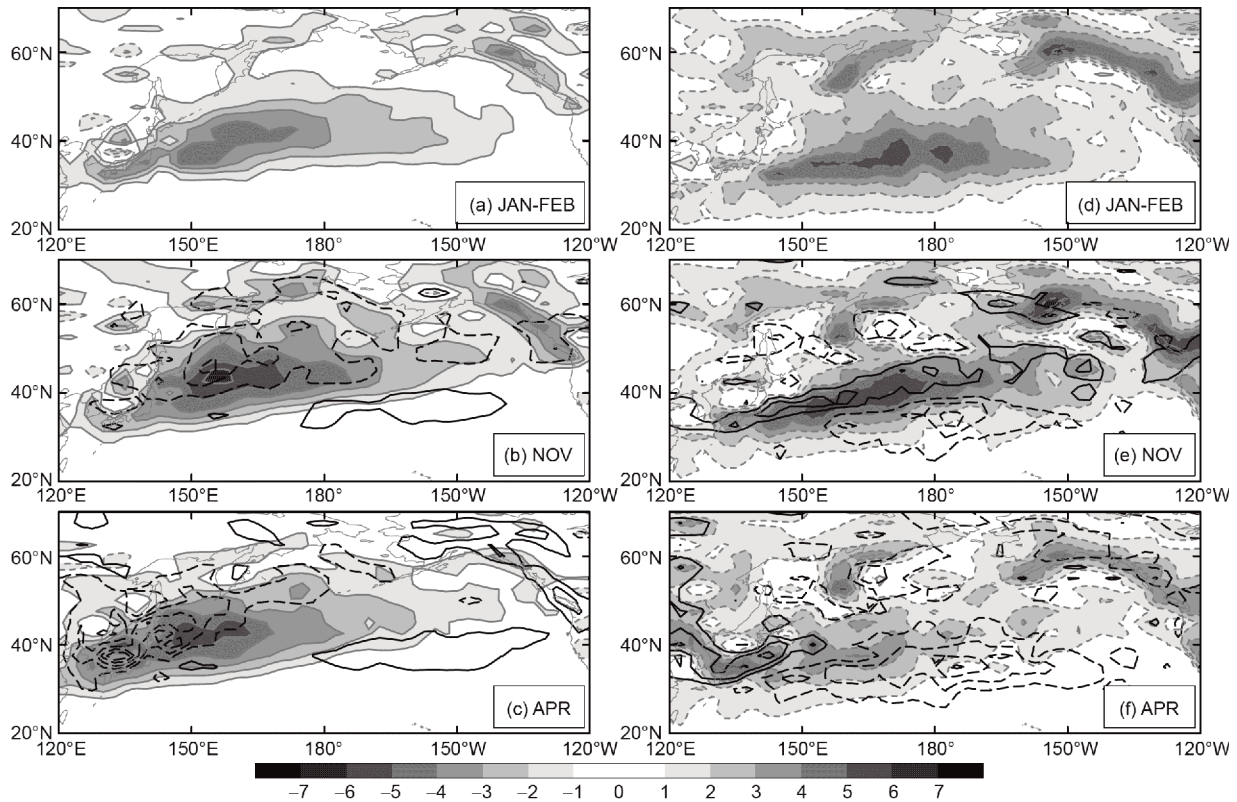


Figure 15 Same as Figure 10, but for (left column) diabatic work (unit: $\text{m}^2 \text{s}^{-3}$) and (right column) friction dissipation (unit: $\text{m}^2 \text{s}^{-3}$). Negative contours are indicated with dashed lines (zero contour omitted). The contour interval is $1 \text{ m}^2 \text{s}^{-3}$.

midwinter minimum (MWM). Based on the European Center Mid-term Weather Forecast Reanalysis Data (ERA-40), this study provides a relatively comprehensive diagnosis of the dynamic causes underlying it, using the recently developed functional analysis tool namely multi-scale window transform (MWT), and the MWT-based localized multi-scale energetics analysis (MS-EVA), together with a feature-tracking technique. By the diagnostic results the phenomenon of MWM is not determined by some single mechanism. Rather, it results from a multitude of mechanisms, including baroclinic canonical transfer, diabatic work, energy flux divergence, and frictional dissipation. The roles of some individual mechanisms, e.g., baroclinic transfer in the traditional sense (Nakamura, 1992; Chen et al., 2013), diabatic processes (Chang, 2001; Lee et al., 2011), have been discussed separately in the literature, but their resultant effect has not been considered before. Besides, in this study we emphasized the effect of canonical energy transfer, not the transfer in the traditional sense.

We found that the multiscale energetics of the Pacific storm track are not symmetric in the seasonal cycle. The energetic scenario in late fall is different from that in early spring. Specifically, baroclinic canonical transfer and diabatic work are maximized in late fall (November), so more TAPE are generated and then converted into TKE through buoyancy conversion, leading to an energy peak in late fall.

The peak of the storm-track strength in early spring (April) is mainly due to the enhancement of eddy energy flux convergence and the reduction of frictional dissipation. It is found that, although baroclinic canonical transfer and buoyancy conversion are weak in early spring, eddy energy flux convergence is very strong, causing a strong net energy inflow into the Pacific storm track. Meanwhile, frictional dissipation is greatly reduced, and is thus beneficial to the long-term maintenance of eddy energy.

The seasonal variation of canonical energy transfer strength is related to the north-south migration of the Pacific jet stream. The Pacific jet stream moves northward and southward as the season marches, and reaches the southernmost point in winter. In contrast, the latitude of the Pacific storm trajectory center is relatively fixed, located in the middle and high latitudes. The jet and storm-track centers are thus far apart in winter, leading to a relatively weak interaction between them. The result is, although the jet stream is strongest in winter, the baroclinic and barotropic canonical transfers are comparatively weak.

The spring enhancement of energy flux convergence in the storm-track region is actually due to the enhancement of the upstream seeding. Storm statistics show that the number and intensity of storms entering the Pacific Storm track from the upstream are maximized in early spring, consistent with the upstream seeding mechanism proposed by Penny et al.

(2010, 2011, 2013).

We remark that, though this present study provides a relatively comprehensive diagnosis of the underlying dynamic processes and causes of the MWM from the perspective of the interaction between the jet stream and synoptic storms, it does not consider the role of the low-frequency atmospheric variations. Previous studies have shown there does exist a close relation between the storm-track variability and the atmospheric low-frequency variability (e.g., Zhu and Sun, 2000; Han et al., 2007; Lau, 1988; Branstator, 1992; Athanasiadis et al., 2010; Wettstein and Wallace, 2010); the latter may affect the storm track through changing the jet stream. We remark that this cannot be skipped before a complete story can be told about the formation of MWM, and are therefore working on it.

Acknowledgements Yuanbing ZHAO thanks Brandon J. Bethel for his help. This work was supported by the National Program on Global Change and Air-Sea Interaction (Grants No. GASI-IPOVAI-06), the Jiangsu Provincial Government through the 2015 Jiangsu Program for Innovation Research and Entrepreneurship Groups and the Jiangsu Chair Professorship to XSL, and the National Natural Science Foundation of China (Grants Nos. 41276032 and 41705024).

References

- Anderson D, Hodges K I, Hoskins B J. 2003. Sensitivity of feature-based analysis methods of storm tracks to the form of background field removal. *Mon Weather Rev*, 131: 565–573
- Athanasiadis P J, Wallace J M, Wettstein J J. 2010. Patterns of wintertime jet stream variability and their relation to the storm tracks. *J Atmos Sci*, 67: 1361–1381
- Branstator G. 1992. The maintenance of low-frequency atmospheric anomalies. *J Atmos Sci*, 49: 1924–1946
- Blackmon M L, Wallace J M, Lau N C, Mullen S L. 1977. An observational study of the Northern Hemisphere wintertime circulation. *J Atmos Sci*, 34: 1040–1053
- Cai M, Yang S, Van Den Dool H M, Kousky V E. 2007. Dynamical implications of the orientation of atmospheric eddies: A local energetics perspective. *Tellus A*, 59, doi: 10.1111/j.1600-0870.2006.00213.x
- Chang E K M. 1993. Downstream development of baroclinic waves as inferred from regression analysis. *J Atmos Sci*, 50: 2038–2053
- Chang E K M. 2001. GCM and observational diagnoses of the seasonal and interannual variations of the Pacific storm track during the cool season. *J Atmos Sci*, 58: 1784–1800
- Chang E K M. 2003. Midwinter suppression of the Pacific storm track activity as seen in aircraft observations. *J Atmos Sci*, 60: 1345–1358
- Chang E K M, Zurita-Gotor P. 2007. Simulating the seasonal cycle of the Northern Hemisphere storm tracks using idealized nonlinear storm-track models. *J Atmos Sci*, 64: 2309–2331
- Chang E K M, Guo Y. 2011. Comments on “The source of the midwinter suppression in storminess over the North Pacific”. *J Clim*, 24: 5187–5191
- Chang E K M, Guo Y. 2012. Is Pacific storm-track activity correlated with the strength of upstream wave seeding? *J Clim*, 25: 5768–5776
- Chang E K M, Lee S, Swanson K L. 2002. Storm track dynamics. *J Clim*, 15: 2163–2183
- Charney J G. 1947. The dynamics of long waves in a baroclinic westerly current. *J Meteorol*, 4: 136–162
- Chen S J, Kuo Y H, Zhang P Z, Bai Q F. 1991. Synoptic climatology of cyclogenesis over East Asia, 1958–1987. *Mon Weather Rev*, 119: 1407–1418
- Chen Y N, Zhu W J, Yuan K. 2013. An energy analysis of midwinter suppression of the North Pacific storm track (in Chinese). *Trans Atmos Sci*, 36: 725–733
- Christoph M, Ulbrich U, Speth P. 1997. Midwinter suppression of Northern Hemisphere storm track activity in the real atmosphere and in GCM experiments. *J Atmos Sci*, 54: 1589–1599
- Chung Y S, Hage K D, Reinelt E R. 1976. On lee cyclogenesis and airflow in the Canadian Rocky mountains and the East Asian mountains. *Mon Weather Rev*, 104: 879–891
- Deng Y, Mak M. 2005. An idealized model study relevant to the dynamics of the midwinter minimum of the Pacific storm track. *J Atmos Sci*, 62: 1209–1225
- Deng Y, Mak M. 2006. Nature of the differences in the intraseasonal variability of the Pacific and Atlantic storm tracks: A diagnostic study. *J Atmos Sci*, 63: 2602–2615
- Eady E T. 1949. Long waves and cyclone waves. *Tellus*, 1: 33–52
- Farrell B. 1984. Modal and non-modal baroclinic waves. *J Atmos Sci*, 41: 668–673
- Han B, Ren X J, Yang X Q. 2007. Analysis of the North Pacific storm track anomaly and the relationship with zonal wind (in Chinese). *J Meteorol Sci*, 27: 237–245
- Harnik N, Chang E K M. 2004. The effects of variations in jet width on the growth of baroclinic waves: Implications for midwinter Pacific storm track variability. *J Atmos Sci*, 61: 23–40
- Hodges K I. 1994. A general method for tracking analysis and its application to meteorological data. *Mon Weather Rev*, 122: 2573–2586
- Hodges K I. 1995. Feature tracking on the unit sphere. *Mon Weather Rev*, 123: 3458–3465
- Hodges K I. 1999. Adaptive constraints for feature tracking. *Mon Weather Rev*, 127: 1362–1373
- Hoskins B J, Hodges K I. 2002. New perspectives on the Northern Hemisphere winter storm tracks. *J Atmos Sci*, 59: 1041–1061
- Lau N C. 1988. Variability of the observed midlatitude storm tracks in relation to low-frequency changes in the circulation pattern. *J Atmos Sci*, 45: 2718–2743
- Lee S S, Lee J Y, Ha K J, Wang B, Kitoh A, Kajikawa Y, Abe M. 2013. Role of the Tibetan plateau on the annual variation of mean atmospheric circulation and storm-track activity. *J Clim*, 26: 5270–5286
- Lee S S, Lee J Y, Wang B, Jin F F, Lee W J, Ha K J. 2011. A comparison of climatological subseasonal variations in the wintertime storm track activity between the North Pacific and Atlantic: Local energetics and moisture effect. *Clim Dyn*, 37: 2455–2469
- Liang X S. 2016. Canonical transfer and multiscale energetics for primitive and quasigeostrophic atmospheres. *J Atmos Sci*, 73: 4439–4468
- Liang X S, Anderson D G M. 2007. Multiscale window transform. *Multiscale Model Simul*, 6: 437–467
- Liang X S, Robinson A R. 2005. Localized multiscale energy and vorticity analysis. *Dyn Atmos Oceans*, 38: 195–230
- Liang X S, Robinson A R. 2007. Localized multi-scale energy and vorticity analysis. *Dyn Atmos Oceans*, 44: 51–76
- Lim G H, Wallace J M. 1991. Structure and evolution of baroclinic waves as inferred from regression analysis. *J Atmos Sci*, 48: 1718–1732
- Lindzen R S, Farrell B. 1980. A simple approximate result for the maximum growth rate of baroclinic instabilities. *J Atmos Sci*, 37: 1648–1654
- Lorenz E N. 1955. Available potential energy and the maintenance of the general circulation. *Tellus*, 7: 157–167
- Ma J, Liang X S. 2017. Multiscale dynamical processes underlying the wintertime Atlantic blockings. *J Atmos Sci*, 74: 3815–3831
- Nakamura H. 1992. Midwinter suppression of baroclinic wave activity in the Pacific. *J Atmos Sci*, 49: 1629–1642
- Nakamura H, Sampe T. 2002. Trapping of synoptic-scale disturbances into the North-Pacific subtropical jet core in midwinter. *Geophys Res Lett*, 29: 8-1–8-4
- Nakamura H, Izumi T, Sampe T. 2002. Interannual and decadal modulations recently observed in the Pacific storm track activity and East Asian winter monsoon. *J Clim*, 15: 1855–1874

- Newton C W. 2004. Associations between twice-yearly oscillations of the North Pacific cyclone track and upper-tropospheric circulations over the eastern hemisphere. *Mon Weather Rev*, 132: 348–367
- Park H S, Chiang J C H, Son S W. 2010. The role of the central Asian mountains on the midwinter suppression of North Pacific storminess. *J Atmos Sci*, 67: 3706–3720
- Penny S, Roe G H, Battisti D S. 2010. The source of the midwinter suppression in storminess over the North Pacific. *J Clim*, 23: 634–648
- Penny S M, Roe G H, Battisti D S. 2011. Reply. *J Clim*, 24: 5192–5194
- Penny S M, Battisti D S, Roe G H. 2013. Examining mechanisms of variability within the Pacific storm track: Upstream seeding and jet-core strength. *J Clim*, 26: 5242–5259
- Pettersen S, Smebye S J. 1971. On the development of extratropical cyclones. *Q J R Met Soc*, 97: 457–482
- Pierrehumbert R T, Swanson K L. 1995. Baroclinic instability. *Annu Rev Fluid Mech*, 27: 419–467
- Robinson D P, Black R X. 2005. The statistics and structure of subseasonal midlatitude variability in NASA GSFC GCMs. *J Clim*, 18: 3294–3316
- Robinson D P, Black R X. 2006. Baroclinic development in observations and NASA GSFC general circulation models. *Mon Weather Rev*, 134: 1161–1173
- Simmons A J, Hoskins B J. 1978. The life cycles of some nonlinear baroclinic waves. *J Atmos Sci*, 35: 414–432
- Strang G, Nguyen T. 1997. *Wavelets and Filter Banks*. Wellesley-Camb Press. 520
- Uppala S M, KÅllberg P W, Simmons A J, Andrae U, Bechtold V D C, Fiorino M, Gibson J K, Haseler J, Hernandez A, Kelly G A, Li X, Onogi K, Saarinen S, Sokka N, Allan R P, Andersson E, Arpe K, Balmaseda M A, Beljaars A C M, Berg L V D, Bidlot J, Bormann N, Caires S, Chevallier F, Dethof A, Dragosavac M, Fisher M, Fuentes M, Hagemann S, Hólm E, Hoskins B J, Isaksen I, Janssen P, Jenne R, McNally A P, Mahfouf J F, Morcrette J J, Rayner N A, Saunders R W, Simon P, Sterl A, Trenberth K E, Untch A, Vasiljevic D, Viterbo P, Woollen J. 2005. The ERA-40 re-analysis. *Q J R Meteorol Soc*, 131: 2961–3012
- Wang C C, Rogers J C. 2001. A composite study of explosive cyclogenesis in different sectors of the North Atlantic. Part I: Cyclone structure and evolution. *Mon Weather Rev*, 129: 1481–1499
- Wang L, Liang X S. 2017. A diagnosis of some dynamical processes underlying a higher-latitude typhoon using the multiscale window transform. *Atmosphere*, 8: 118
- Wettstein J J, Wallace J M. 2010. Observed patterns of month-to-month storm-track variability and their relationship to the background flow. *J Atmos Sci*, 67: 1420–1437
- Xu F, Liang X S. 2017. On the generation and maintenance of the 2012/13 sudden stratospheric warming. *J Atmos Sci*, 74: 3209–3228
- Yang Y, Liang X S. 2016. The instabilities and multiscale energetics underlying the mean-interannual-eddy interactions in the Kuroshio extension region. *J Phys Oceanogr*, 46: 1477–1494
- Yao Y, Zhong Z, Yang X Q. 2018. Influence of the subarctic front intensity on the midwinter suppression of the North Pacific storm track. *Dyn Atmos Oceans*, 81: 63–72
- Yin J H. 2002. The peculiar behavior of baroclinic waves during the midwinter suppression of the Pacific storm track. Doctoral Dissertation. University of Washington. 137
- Zhang Y. 1997. On the mechanisms for the mid-winter suppression of the Pacific storm track. Doctoral Dissertation. Princeton: University of Princeton
- Zhang Y, Held I M. 1999. A linear stochastic model of a GCM's mid-latitude storm tracks. *J Atmos Sci*, 56: 3416–3435
- Zhao Y B, Liang X S. 2018. On the inverse relationship between the boreal wintertime Pacific jet strength and storm-track intensity. *J Clim*, 31: 9545–9564
- Zhao Y B, Liang X S, Gan J. 2016. Nonlinear multiscale interactions and internal dynamics underlying a typical eddy-shedding event at Luzon Strait. *J Geophys Res-Oceans*, 121: 8208–8229
- Zhu W J, Sun Z B. 1999. A review on storm track research (in Chinese). *J Nanjing Inst Meteorol*, 22: 121–127
- Zhu W J, Sun Z B. 2000. Interannual variability of northern winter Pacific storm track and its association with 500 hPa height and tropical and northern Pacific sea surface temperature (in Chinese). *Acta Meteorol Sin*, 58: 309–320

(Responsible editor: Dehai LUO)